An Integrated Evaporator for Efficient Solar-Driven Interfacial Steam Generation

Journal:	*Nano Letters*
Manuscript ID	nl-2020-019994.R3
Manuscript Type:	Communication
Date Submitted by the Author:	18-Jul-2020
Complete List of Authors:	Chen, Jinxing; University of California Riverside Li, Bo; Jilin University, Key Laboratory of Bionic Engineering(Ministry of Education) Hu, Guoxiang; University of California Riverside Aleisa, Rashed; University of California Riverside Lei, Shan; University of Science and Technology of China Yang, Fan; University of California Riverside Liu, Dilong; University of California Riverside Lyu, Fenglei; Institute of Functional Nano and Soft Materials, Wang, Mozhen; University of Science and Technology of China, Department of Polymer Science and Engineering Ge, Xuewu; University of Science and Technology of China, Department of Polymer Science & Engineer Qian, Fang; Lawrence Livermore National Laboratory, Physical and Life Sciences Directorate Zhang, Qiao; Soochow University, Yin, Yadong; University of California Riverside,

An Integrated Evaporator for Efficient Solar-Driven Interfacial Steam Generation

Jinxing Chen[1, 2, 3], Bo Li[2], Guoxiang Hu[4], Rashed Aleisa[2], Shan Lei[3], Fan Yang[2], Dilong Liu[2], Fenglei Lyu[1], Mozhen Wang[3], Xuewu Ge[3], Fang Qian[5], Qiao Zhang[1], and Yadong Yin[2]**

[1] Institute of Functional Nano & Soft Materials (FUNSOM), Jiangsu Key Laboratory for Carbon-Based Functional Materials & Devices, Soochow University, Suzhou, Jiangsu 215123, P.R. China

[2] Department of Chemistry, University of California, Riverside, CA 92521, USA

[3] CAS Key Laboratory of Soft Matter Chemistry, Department of Polymer Science and Engineering, University of Science and Technology of China, Hefei, Anhui 230026, P.R. China

[4] Center for Nanophase Materials Sciences, Oak Ridge National Laboratory, Oak Ridge, Tennessee 37831, USA

[5] Physical and Life Sciences Directorate, Lawrence Livermore National Laboratory, Livermore, CA 94550, USA

KEYWORDS: solar steam generation, interfacial evaporation, polypyrrole microsheets, desalination, photothermal effect

Abstract: Solar-driven interfacial steam generation is a promising technique for clean water production as it can minimize thermal loss by localizing solar-to-heat conversion at the air/liquid interface. Here we report an integrated solar-evaporator by partially growing two-dimensional polypyrrole microsheets within a melamine foam through chemical vapor polymerization. These microsheets can induce multiple light reflections within the foam, enable omnidirectional light

absorption, provide abundant surfaces to promote heat transfer, and achieve spatially-defined hydrophobicity to facilitate vapor escape. Meanwhile, the inherent hydrophilicity of the bottom part of the foam promotes spontaneous upward water transport and suppresses heat loss. The composite foam exhibits an excellent apparent evaporation rate of ~2 kg/(m^2·h) and solar-to-vapor efficiency of ~91%. The combined advantages of large surface area, high efficiency, low cost, all-weather application, excellent durability, and scalable manufacturing make our integrated design promising for fabricating large-scale solar steam generation systems that are suitable for practical clean water production.

Keywords: interfacial steam generation; photothermal effect; integrated evaporator; polypyrrole; melamine foam

Solar-driven interfacial steam generation (SISG), which localizes solar heating at the air-water interface, has recently emerged as a new technology to access clean water for everyday use, especially in areas where freshwater resources are scarce.[1-4] Localized heating at the air-water interface instead of bulk heating enables higher solar-to-vapor conversion efficiency and lesser utilization of photothermal materials.[5-8] Compared with traditional seawater purification technologies such as reverse osmosis and ion exchange, the SISG evaporator can improve the solar-to-vapor conversion efficiency to as high as 90 %, which potentially enables the design of home-scale SISG devices for generating fresh water at a rate of 2.5 L·m^{-2}·d^{-1}, sufficient for meeting individual daily drinking needs.[9]

Previous fundamental studies have revealed three key principles for designing high-performance SISG: (1) employing photothermal materials with broadband absorption to maximize solar-to-heat

conversion; (2) localizing heating at the evaporative region to minimize heat loss; (3) supplying sufficient water by porous and hydrophilic structures to support continuous evaporation.[10, 11] Typically, plasmonic nanoparticles, graphene, or semiconductor nanoparticles are used as the photothermal materials to enhance solar-to-heat conversion, although there are drawbacks in scalability, price, and portability.[12, 13] Despite the relatively compact size of the active materials, the evaporator design has to incorporate a bulky underlying layer for thermal insulation and water transportation. The development of simple yet more efficient SISG systems is critical to expedite solar-steam generation techniques toward real-world applications.

Hydrophilic open-cell melamine foam (MF) combines excellent thermal insulating and water transport properties,[14-17] and it holds great potential for large-scale applications due to its low cost, high evaporation surface area, high flexibility, and commercial large-scale availability. However, commercial MF has limited uses in solar steam generation as it suffers from poor solar-to-heat conversion efficiency.[16, 17] In this work, we report an integrated design of Janus-structured MF for highly efficient solar steam generation. The unique Janus structure is created by partially modifying the top layer of an MF with two-dimensional (2D) polypyrrole (PPy) microsheets through vapor phase polymerization of pyrrole on $FeCl_3$ films, which are pre-formed inside the MF (bounded by the skeletons). In addition to forming microsheets, PPy also coats the skeletons, thus significantly improves light absorption without affecting the water transport inside the foam. As a result, the top region of the Janus structure can achieve broadband absorption to maximize solar utilization, as well as spatially-defined hydrophobicity to facilitate vapor escape. Meanwhile, the bottom part of the MF retains its inherent hydrophilicity and abundant porosity, promoting spontaneous upward water transport and suppressing heat loss. This integrated design achieves a very high steam generation rate of ~2 $kg/m^2 \cdot h$ with solar-to-water conversion efficiency up to 90%,

which, in combination with the intrinsic features of both MF and PPy such as low cost, high scalability, and excellent durability, provides broad prospects for producing potable water to meet the daily needs of individuals in water-stressed locations.

Commercial MFs typically have a porosity of up to 99.99%. Introduction of PPy, a dark-colored conjugated polymer to an MF can improve light absorption. However, if only a layer of photothermal conversion material (PPy) is coated on the surface of the skeletons, the mass loading is still very low, resulting in inefficient solar-to-heat conversion. To increase the loading of PPy and its contact area with water without affecting the water transport inside the foam, we first introduce 2D PPy microsheets inside the foam by taking advantage of a unique property of $FeCl_3$, that is, the spontaneous formation of $FeCl_3$ thin films or microsheets upon drying its ethanol solution soaked into the foam. The introduced $FeCl_3$, which also coats on the MF skeletons, is then used as an initiator to induce the vapor phase polymerization of pyrrole and cover a layer of PPy on the $FeCl_3$ microsheets and skeletons (**Figure 1a**).

A Janus foam can be prepared by soaking one side of an MF with a $FeCl_3$/ethanol solution (Figure SI-1). Upon evaporation of the solvent, 2D $FeCl_3$ microsheets bounded by the skeletons are formed inside the MF, as schematically illustrated in **Figure 1b.** The typical SEM image and elemental mappings of the products are shown in **Figure 1c**. The strong signals of iron and chlorine and weak signal of carbon indicate that 2D microsheets are composed of $FeCl_3$. The formation of 2D microsheets is unique to $FeCl_3$ (Figure SI-2), and the microsheets were found to be amorphous according to *In-situ* X-ray diffraction (XRD) analysis (Figure SI-3). *In-situ* optical observation showed that the solution gradually increased its viscosity upon drying (Movie S1 and Figure SI-4). **Figure 1d** shows the strong dependence of the solution viscosity on the $FeCl_3$ concentration, which is believed to be responsible for the unique filming behavior. As this behavior is very similar

to that of a typical polymer solution, one would suspect the likelihood of polymerization of the salt at higher concentrations. This mechanism is confirmed by density functional theory (DFT) calculations, which show that the negative binding energy ΔE decreases monotonously as the degree of polymerization increases, indicating that polymerization is a favorable reaction. Experimentally, we also observed that a high concentration of $FeCl_3$ promotes the formation of 2D microsheets. At a concentration (0.5 and 1.0 mg/mL), no obvious 2D $FeCl_3$ microsheets were observed. However, the coverage of 2D $FeCl_3$ microsheets increased with increasing the concentration of $FeCl_3$, covering over 60% of pores at 50 mg/mL (Figure SI-5).

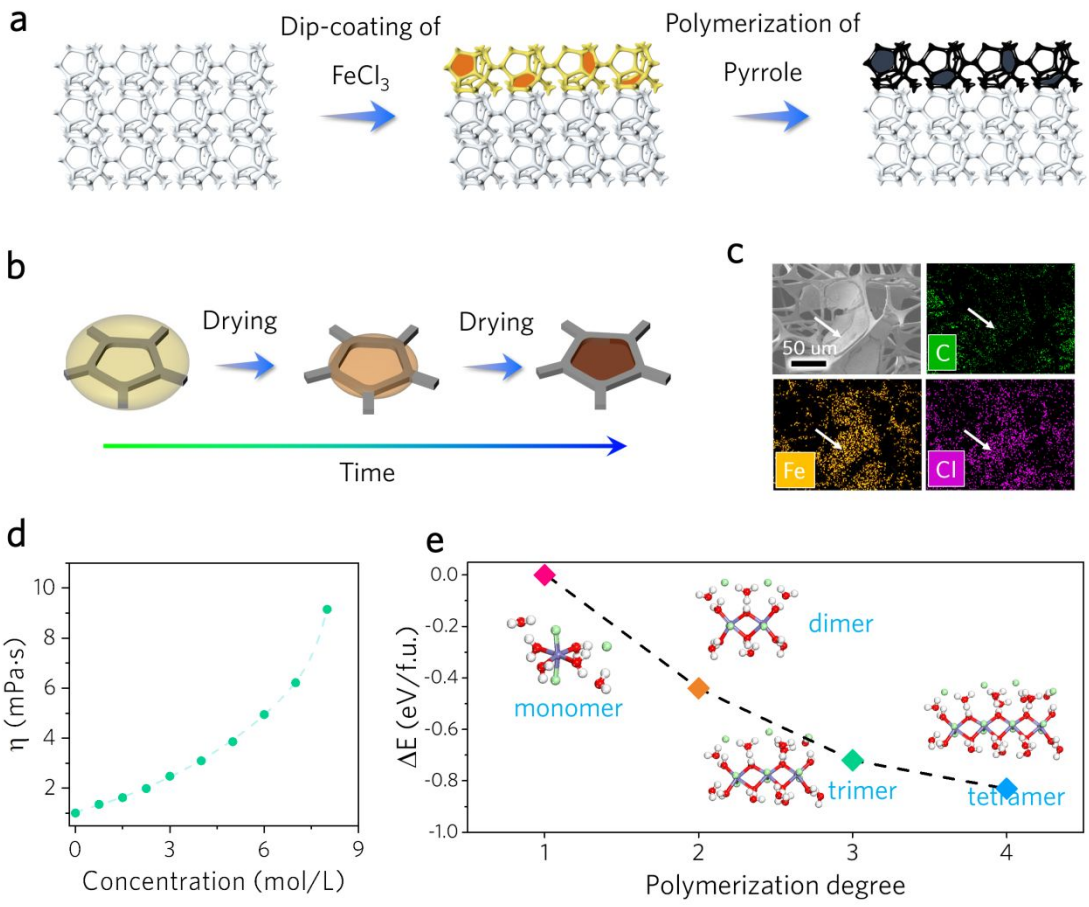

Figure 1. (a) Schematic illustration showing the formation of 2D microsheets by dip-coating of $FeCl_3$/ethanol solution and vapor phase polymerization of pyrrole. (b) Graphical illustration of the formation processes of 2D microsheets. (c) SEM and EDS mappings of 2D microsheets within MF after drying of $FeCl_3$/ethanol solution (25 mg/mL). (d) The correlation between viscosity and concentration of $FeCl_3$. (e) Relative stable energy of $FeCl_3$ oligomers versus polymerization degree.

The above $FeCl_3$-treated foam was then placed into a sealed container and exposed to a pyrrole vapor to initiate its polymerization, producing a Janus structure consisted of a black melamine-PPy foam (MPF) top layer and white MF bottom layer (**Figure 2a**). We found that an MPF with a top layer of 6 mm and a bottom layer of 14 mm showed the best evaporation rate, so this thickness ratio was used as the standard in this study (Figure SI-6). As shown in **Figure 2b**, the original MF shows a high porosity and smooth skeletons, while the MPF displays more complicated structures, where the surface of MF was covered with a thin layer of PPy (middle image in **Figure 2c**) and many PPy microsheets were formed between the skeletons (**Figure 2c**). The elemental mapping analyses in **Figure 2d-2g** show that the 2D materials were composed of carbon and nitrogen with a carbon to nitrogen ratio (C/N) around 4, through sampling three different regions (P1, P2, and P3). This (C/N) ratio was consistent with the theoretical (C/N) ratio in PPy (4:1), confirming that these 2D layered materials were PPy microsheets. It is worth noting that the 2D PPy microsheets can hardly be prepared by other methods such as directly liquid phase polymerization of pyrrole due to the dissolution of $FeCl_3$ in water (Figure SI-7). **Figure 2h** is the cross-sectional view of the interface between the MPF layer (upper region) and the MF layer (bottom region), as highlighted by the yellow dashed line. The elemental mapping of carbon and nitrogen were consistent with the outline of the framework. The upper layer was found to have lower nitrogen and higher carbon

density, which also agreed with the chemical structures of pyrrole (C/N = 4) and melamine (C/N = 0.5).

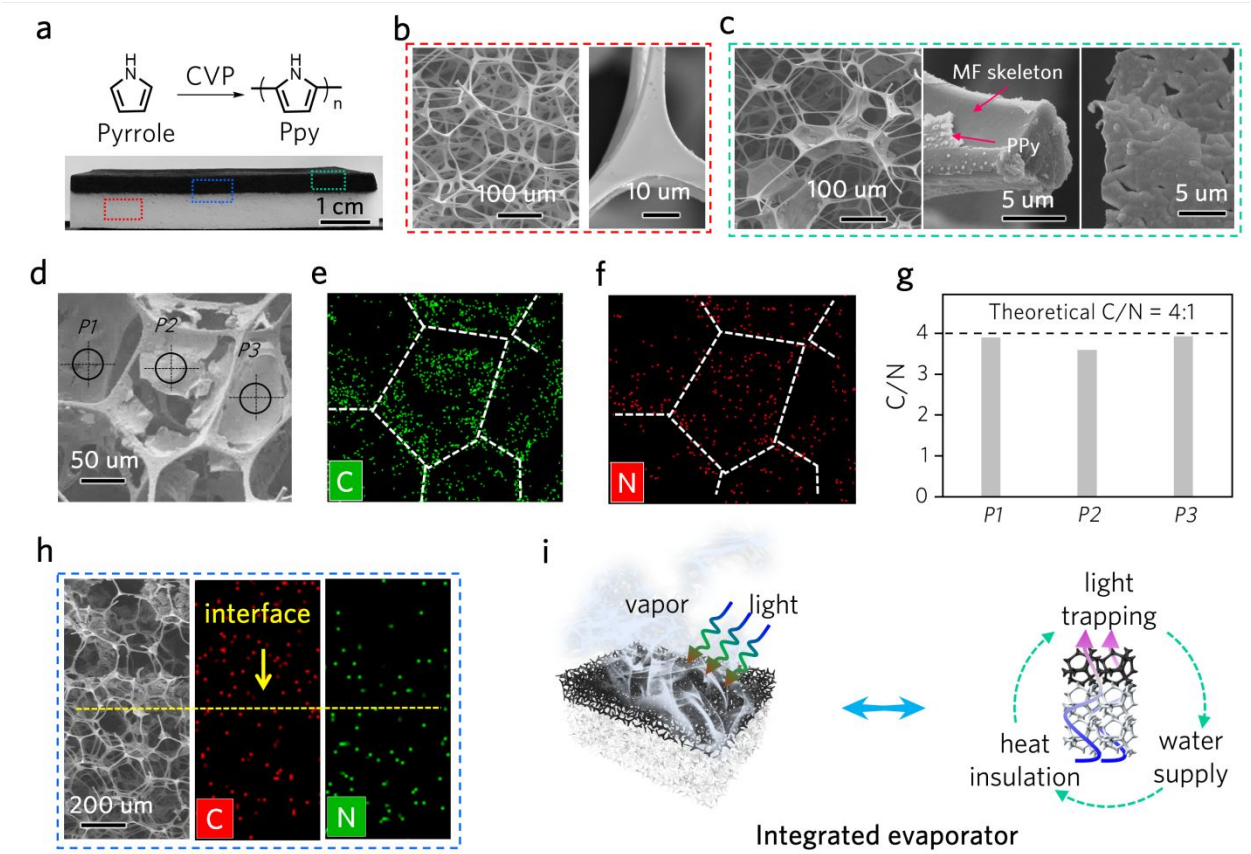

Figure 2. (a) Digital image of an integrated Janus evaporator sample. (b, c) SEM images of the white layer and black layer of composite foam. (d, e, f, g) SEM image, elemental mapping, and carbon to nitrogen ratio of 2D layered nanostructure in MPF after washing with water for four times. (h) SEM image and elemental mapping of the cross-section of the capillary channels at the interface between the MPF and MF layers. (i) Graphical illustration of the integrated solar evaporator.

The number density of 2D PPy microsheets increased with the concentrations of $FeCl_3$ that were used for treating the MF. The samples treated with 0.5, 1, 10, 25, and 50 mg/mL $FeCl_3$ were named

as MPF-0.5, MPF-1, MPF-10, MPF-25, and MPF-50, respectively (Figure SI-8). A careful comparison showed that the number density of PPy microsheets is almost the same as that of the corresponding $FeCl_3$ microsheets, indicating that all $FeCl_3$ microsheets were covered by PPy. The polymerization kinetics showed that the reaction accelerated first then slowed down because of the gradual coverage of the initiators by the deposited PPy layer (Figure SI-9). By comparing the saturated mass loading of PPy in all cases, we found that the $FeCl_3$ microsheets provided more sites for the deposition of PPy, significantly raising its mass loading. The equilibrium temperature of different samples upon illumination increased consistently with increasing the mass loading (Figure SI-10a), reaching a maximum value of ~70 ^oC with MPF-25, with excellent photothermal conversion effect even after 6 cycles (Figure SI-10b).

As summarized in **Figure 2i**, we architected an MF-based integrated Janus-structured evaporator where the top region was PPy covered MF with broadband absorption and hydrophobicity for optimizing light absorption, heat generation, and vapor escape, while the bottom MF region provides a large number of macro-pores and hydrophilic surface that facilitate water transport and reduce thermal loss.

The efficient absorption of solar radiation and its conversion into heat is the critical step to drive water evaporation.[11, 18] The absorption properties of the MPF were measured by a UV–Vis-NIR spectrometer with an integrating sphere (Figure SII-1). The MPF-25 absorbed 98.1% of incident light (weight under AM 1.5 G), while the pure MF had a solar absorption efficiency of 33.1%. Besides the contribution by PPy, the unique porous structure of MPF also helped trap the incident light because the rough surface with many open pores allows the light to travel through the foam and the trapped light goes through multiple reflections within the continuous porous structure (Figure SII-2), which were previously proved to achieve efficient light absorption.[19]

An omnidirectional solar absorber is more favorable for practical applications as the radiation angle of sunlight changes consistently in real-time.[20-22] As shown in **Figure 3a**, we examined the angular dependence of the MPF-25 absorption through angle-resolved spectrometry following three modes: 1) fixing angles of incident light and signal detector to form a mirror reflection mode (**Figure 3b**); 2) changing the signal detector direction from -75^{o} to 75^{o} with the angle of incident light fixed as 45^{o} (**Figure 3c**); 3) rotating MPF-25 along the normal line from 0^{o} to 360^{o} while fixing the angles of incident light and signal detector at -45^{o} and 45^{o}, respectively (with the light spot at the same region, **Figure 3d**). Remarkably, the MPF-25 had a very low reflectance in all cases (less than 5 %). The MPF-25 also exhibited a similar absorption profile in the near-infrared spectral region (Figure SII-3), which confirms its angular-independent absorption property throughout the whole solar spectrum. The unique angular-independent absorption property, which originates from the randomly distributed pores within MF, suggests that the projected densities of the pores are similar regardless of the injected angles of light. **Figure 3e** shows that the MPF-25 also had an angular-independent solar-to-heat conversion property that the surface temperature had negligible variation when the incident angle varies from 30^{o} to 150^{o}. Also, the MPF-25 showed an excellent capability in thermal management due to its low thermal conductivity and thermal radiation (Figures SII-4 and SII-5).

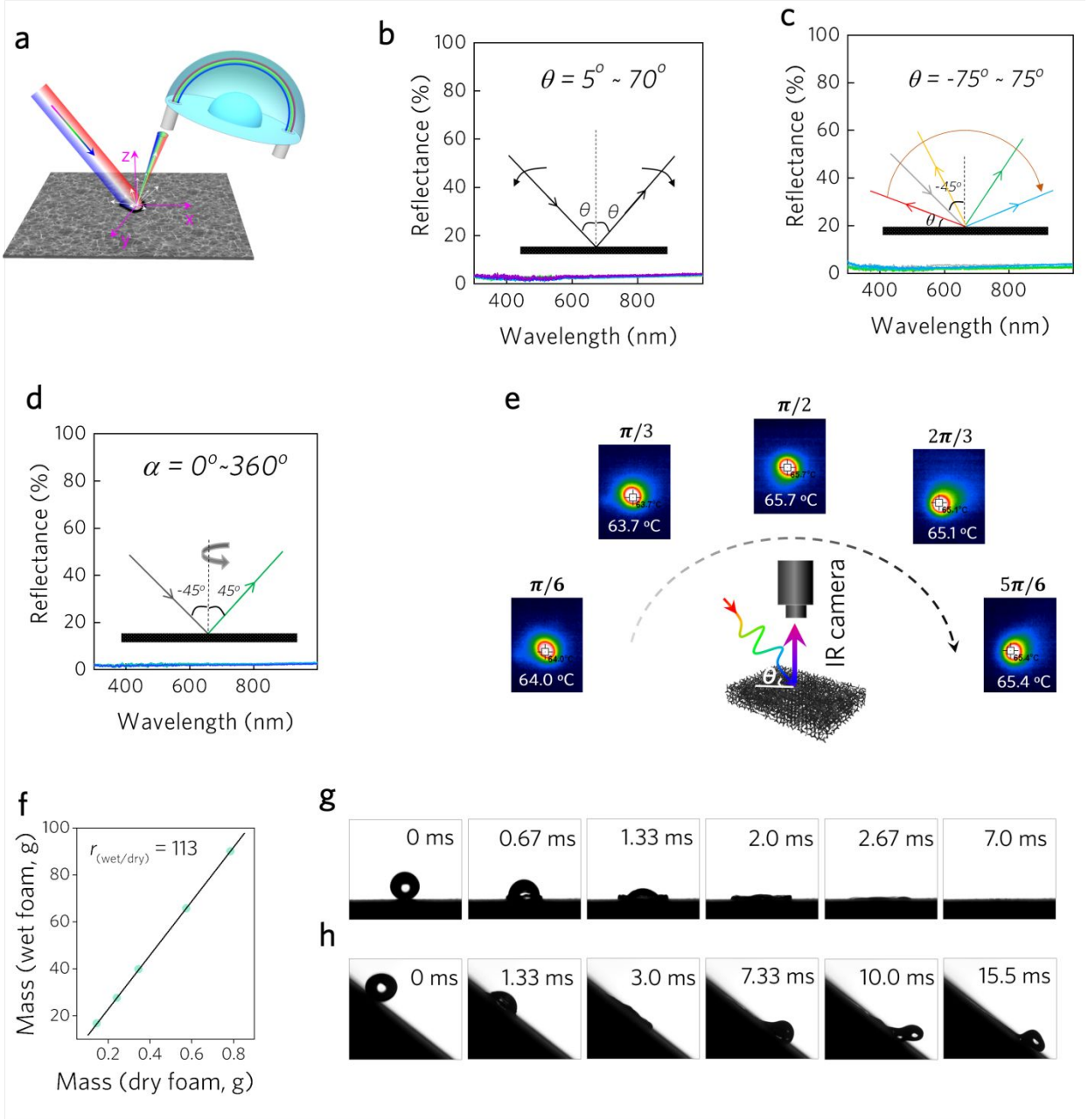

Figure 3. (a-d) Angle-resolved spectrometry characterizing the angular reflectivity property of MPF-25. (e) The relationship between the incident angle of light and the photothermal conversion effect. (f) Water absorption capacity as a function of the mass of the foam. (g, h) Images recorded by a high-speed camera showing the spreading process and movement dynamics of a water droplet on a horizontal MF foam (g) and an MPF foam tilted by 40° (h).

MF exhibits extremely strong water capture ability because of its unique porous structures and excellent wettability. It absorbs water up to 113 times its weight, indicating a high porosity of up to 99% (**Figure 3g**). A high-speed camera system was used to record the spreading process and movement dynamics of water droplets on the hydrophilic MF (**Figure 3h** and movie S2). When a water droplet (~15 μL) fell onto the surface, it spread out quickly, reaching a contact angle near 0°. The whole process completed within 7 ms, suggesting very good water wettability.[23,24] The fast water-absorbing property makes the MF a suitable candidate to provide efficient water supply in the SISG system, which is critical to high-efficiency interfacial evaporation.[25,26]

Conversely, a moderately hydrophobic layer is preferred for water evaporation because it would reduce the evaporation work of water, as described by the following equation (the deduction is shown in Figure S III-1):

$$W_a = \gamma_{lv}(1 + cos\theta) \qquad \text{Equation 1}$$

where W_a is the evaporation work of liquid, γ_{lv} the surface tension of the liquid in equilibrium with the vapor, and θ the static contact angle of liquid. Therefore, the increased water contact angle leads to decreased evaporation work. However, a too hydrophobic surface also hinders water transport within the heating area. A high-speed camera was therefore used to investigate water transportation in the heating layer. The water droplet spread-out quickly after falling on the black side. At about 3 ms, the area of the water film reached a maximum, and then the water film rapidly shrank, retracting finally into a sphere-like droplet within 15.5 ms (**Figure 3i** and movie S3). These images show that MPF has a typical Wenzel wetting behavior and its hydrophobic surface has a considerable affinity to water, thereby facilitating water transfer and evaporation simultaneously.[27]

The steam generation performance of MPFs was quantified by plotting the total mass change due to water evaporation as a function of solar illumination time (**Figure 4a**). Upon light illumination, the bare water showed a relatively small amount of weight loss, while cases with various Janus foams all exhibited dramatic water loss. **Figure 4b** summarizes the relationship between samples and the evaporation rate. The weight loss performance increases in the following order MPF-0.5 < MPF-1.0 < MPF-10 < MPF-50 < MPF-25. Although they share the same temperature rising profile, which suggests the similar solar-to-thermal effect (Figure SI-10a), MPF-25 displays a much higher evaporation performance than MPF-50, because too many PPy microsheets in MPF-50 block the water transport (Figure SIV-1).

To further evaluate the steam generation performance of the Janus foams, we calculated the evaporation efficiency (η) by:

$$\eta = \frac{\dot{m} h_{LV}}{I} \qquad \text{Equation 2}$$

where $\dot{m}$ is the mass flux, I the power density of solar energy, and h_{LV} the equivalent evaporation enthalpy of capillary water. The apparent solar steam generation efficiencies are calculated. As shown in **Figure 4b** (solid stars), the apparent evaporation efficiency exceeded the theoretical value when the evaporation enthalpy of bulk water was used for calculation. In fact, the evaporation enthalpy of water changes when the evaporation occurs at liquid-solid interfaces.[28-31] In our case, the upper layer of MPF-25 is moderately hydrophobic, which makes water easier to escape from the interface (equation 1). We further calculated that the effective evaporation enthalpy of water within MPF-25 is 1710 J/g by controlled experiments, which thereby provides a real solar-to-vapor efficiency of 91.3% for MPF-25, exceeding the most reported results (Table S1). The heat loss due to radiation, conduction, and convection was calculated to be ~3.2%, 3.4%,

and 2.6%, respectively (Figure SIV-2). Therefore, the total heat loss of ~9.2% is consistent with its solar-to-vapor efficiency (~91%). Additionally, increasing the solar energy led to the monotonic increase of evaporation rate, but reaches a maximum efficiency under 2-sun illumination (**Figure 4c**). The significant drop in efficiency at a high optical concentration can be attributed to the maximum light absorption of MPF (Figure SIV-3a). We also compared the steam generation performance of MPF with that of carbonized MF that typically used in other studies.[15-17] The MPF showed a better performance than two carbonized foams under the same test condition (Figure SIV-3b and SIV-3c).

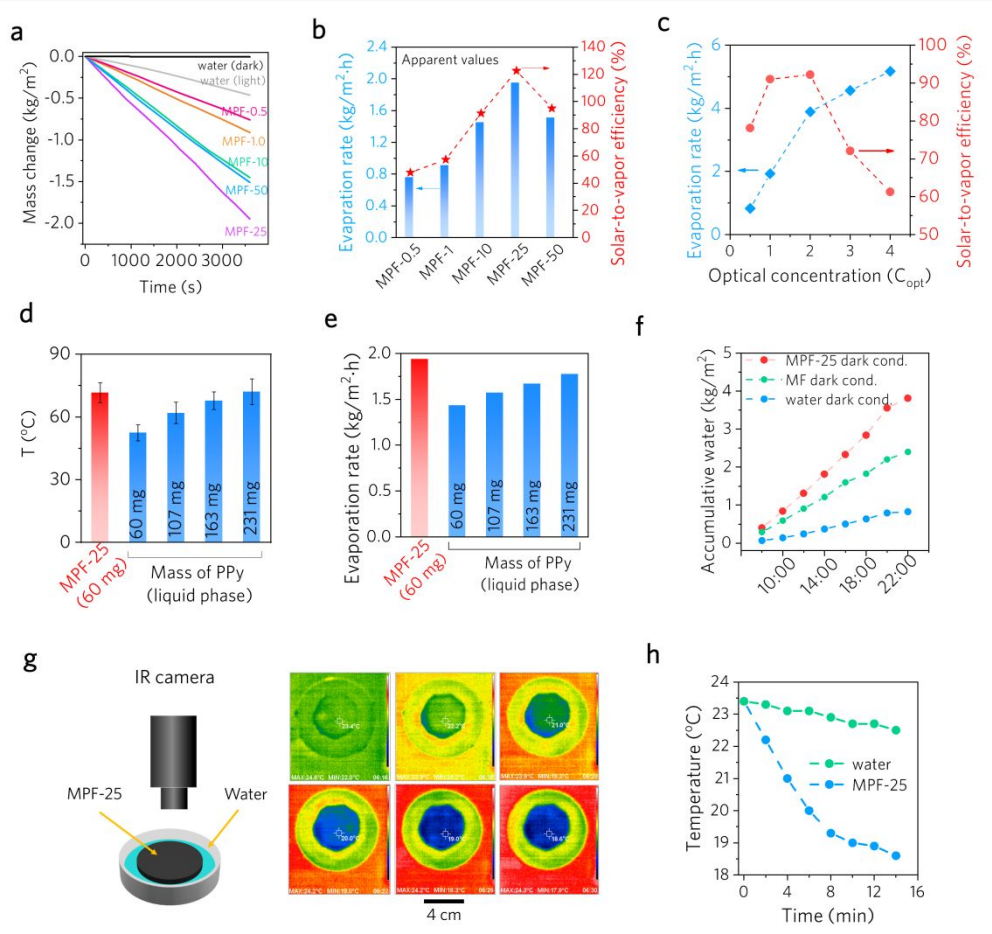

Figure 4. (a) Cumulative weight loss of pure water and the MPFs through water evaporation over time. (b) Evaporation rate and energy efficiency of MPFs. (c) Evaporation rates and energy efficiency of MPF-25 under different optical density. (d) The photothermal conversion effect and (e) steam generation performance of Janus evaporator, prepared by vapor phase polymerization and aqueous phase polymerization with varying mass loading of PPy. (f) Accumulative water loss by standing water or MF and MPF-25 covered water in darkness. (g) The temperature change in a typical evaporation system in darkness. (h) The surface temperatures of water and MPF-25 with different self-evaporation times.

In addition to their contribution to enhancing the solar-to-heat conversion performance,[32, 33] the PPy microsheets also benefit water evaporation. For comparison, we coated PPy on MF without the formation of microsheets using an aqueous phase polymerization by immersing $FeCl_3$-modified MF in an aqueous pyrrole solution (MPF_{liq}). The photothermal conversion effect of MPF-25 (with PPy loading amount of 60 mg) and MPF_{liq} with varying loading amounts of PPy from 60 to 231 mg (MPF_{liq}-60, MPF_{liq}-107, MPF_{liq}-163, and MPF_{liq}-230) were investigated in **Figure 4d**. When the same amount of PPy was used, MPF-25 with the embedded PPy microsheets showed more obvious temperature enhancement than MPF_{liq}, thanks to the enhanced multiple light reflection caused by the microsheets.[20] The difference in temperature can be compensated by increasing the amount of PPy in MPF_{liq}, showing a similar photothermal conversion effect to MPF-25 when the MPF_{liq} has a mass loading of 230 mg. Although MPF-25 and MPF_{liq}-230 share a similar temperature increase, the MPF-25 produced more vapor than that of MPF_{liq}-230 (**Figure 4e**), indicating a better water evaporation efficiency of MPF-25 due to the presence of more heating sites of 2D PPy sheets.

During the experiments, we found that covering with MPF-25 on water in darkness showed an obvious water loss (0.457 kg/m^2·h), comparable with water under illumination with 1 sun (0.461 kg/m^2·h, **Figure 4a**). We further tested the accumulative weight loss of water with and without MPF-25 in a dark and open system with a humidity of ~27%. The covering with MPF-25 achieved a weight loss of ~3.81 kg/m^2 within 14 h (**Figure 4f**) while the control group of MF-water and water showed ~2.39 and ~0.83 kg/m^2 of water loss under the same conditions. During the dark evaporation, a lower surface temperature of MPF-25 than the surrounding environment in dark also proves its high evaporation rate. (**Figures 4g, 4h,** SIV-5). In principle, such an evaporation rate alone could meet an individual's daily drinking needs, providing there is an efficient method for collecting the evaporated water. It's worthy to note that in more practical situations such as in cloudy weather or night time, the MPF-25 may still be used to generate clean water, demonstrating its potential as an all-weather/time clean water generator, which hasn't been reported previously.

The MPF-25 also demonstrated its excellent performance in practical solar desalination (Figure SIV-6 and SIV-7). The salinity of purified water was approximately two orders of magnitude below the drinking water stands defined by the World Health Organization (WHO, 0.1%) and the US Environmental Protection Agency (EPA, 0.05%). The concentrations of all four primary ions (Na^+, Mg^{2+}, K^+ and Ca^{2+}) present in the seawater were significantly reduced, which were below the values typically obtained through membrane-based (10–500 mg/L) and thermal distillation-based (1–50 mg/L) seawater desalination techniques. Besides, the MPF-25 features the high mechanical and thermal stability (Figure SIV-8), good ultraviolet aging resistance (Figure SIV-9), and regenerable salt-rejection abilities (Figure SIV-10), which are important aspects of practical desalination applications. It must be noted that MF has a low density of 9.19 kg/m^3 (only 7.5-fold higher than air, which promises substantial savings of its storage and transportation. Also, scaling-

up the fabrication of MPF is highly feasible (Figure SIV-11). We estimated that the total materials cost for each membrane (1 m^2) is only $ 2.6 (Table S2). All these features are of great advantage for practical clean water production for human daily drinking.

In conclusion, we report the development of a Janus-structured heat localizing solar-evaporator by partially modifying a commercial melamine foam with two-dimensional polypyrrole microsheets. These two-dimensional microsheets can achieve high photothermal-conversion efficiency and provide abundant surface area to promote heat transfer to surrounding water molecules, as well as make the top layer of the foam hydrophobic, which facilitates water evaporation. The unmodified bottom possesses excellent water transport and thermal insulation properties. Furthermore, due to the unique Janus wettability, the composite foam allows spontaneous water evaporation even in the absence of light irradiation, demonstrating its potential for all-weather applications. The combined advantages of high efficiency, low price, excellent durability, industry-compatible and scalable manufacturing process, and commercially available precursors make our integrated design promising for fabricating large-scale solar steam generation systems that are suitable for practical clean water production.

ASSOCIATED CONTENT

Supporting Information. The following files are available free of charge. Materials and methods: foam fabrication technique, material characterization and solar steam generation test; supplementary Figures; Table S1-S2.

AUTHOR INFORMATION

Corresponding Author

Yadong Yin

Email: yadong.yin@ucr.edu

Qiao Zhang

Email: qiaozhang@suda.edu.cn

Author Contributions

Y.Y. and J.C. conceived and designed the experiments. J.C. and B.L. synthesized materials and contributed equally to this work. G.H. conducted the DFT calculation. S.L., D.L., L.F., M.W., and X.G. contributed to sample characterization. F.Q., J.C., Q.Z. and Y.Y. analyzed the results and wrote the manuscript. R.A. and F.L. also revised the manuscript. The manuscript was written through the contributions of all authors.

ACKNOWLEDGMENT

This work was supported partially by the National Natural Science Foundation of China (21703146, 51901147, 51922073), and the Natural Science Foundation of Jiangsu Province (BK20180097), and the China Postdoctoral Science Foundation (2019M651939). This work was also supported in part by the USDA National Institute of Food and Agriculture (Award No: 2020-65210-30764). Qian also acknowledge the support by Lawrence Livermore National Laboratory under the auspices of the U.S. Department of Energy under Contract No. DE-AC52-07NA27344. The authors are also grateful for the kind assistance from Ideaoptics Inc. on the angle-resolved spectrum measurements.

REFERENCES

(1) Ren, H.; Tang, M.; Guan, B.; Wang, K.; Yang, J.; Wang, F.; Wang, M.; Shan, J.; Chen, Z.; Wei, D.; Peng, H.; Liu, Z. Hierarchical Graphene Foam for Efficient Omnidirectional Solar-Thermal Energy Conversion. *Adv. Mater.* **2017**, *29*, 1702590.

(2) Tao, P.; Ni, G.; Song, C.; Shang, W.; Wu, J.; Zhu, J.; Chen, G.; Deng, T. Solar-Driven Interfacial Evaporation. *Nat. Energy* **2018**, *3*, 1031–1041.

(3) Zhou, X.; Guo, Y.; Zhao, F.; Yu G. Hydrogels as an Emerging Material Platform for Solar Water Purification. *Acc. Chem. Res*. **2019**, *52*, 3244–3253.

(4) Zhou, X.; Zhao, F.; Guo, Y.; Rosenberger, B.; Yu, G. Architecting Highly Hydratable Polymer Networks to Tune the Water State for Solar Water Purification. *Sci. Adv.* **2019**, *5*, eaaw5484.

(5) Zhou, L.; Tan, Y.; Wang, J.; Xu, W.; Yuan, Y.; Cai, W.; Zhu, S.; Zhu, J. 3D Self–Assembly of Aluminium Nanoparticles for Plasmon–Enhanced Solar Desalination. *Nat. Photonics* **2016**, *10*, 393–398.

(6) Strachan, N.; Fais, B.; Daly, H. Reinventing the Energy Modelling-Policy Interface. *Nat. Energy* **2016**, *1*, 16012.

(7) Ghasemi, H.; Ni, G.; Marconnet, A. M.; Loomis, J.; Yerci, S.; Miljkovic, N.; Chen, G. Solar Steam Generation by Heat Localization. *Nat. Commun.* **2014**, *5*, 4449.

(8) Zhao, F.; Guo, Y.; Zhou, X.; Shi W.; Yu G. Materials for Solar-Powered Water Evaporation. *Nat. Rev. Mater*. **2020**, *5*, 388–401.

(9) Ni, G.; Zandavi, S. H.; Javid, S. M.; Boriskina, S. V.; Cooper, T. A.; Chen, G. A Salt-Rejecting Floating Solar Still for Low–Cost Desalination. *Energy Environ. Sci.* **2018**, *11*, 1510–1519.

(10) Chen, J.; Feng, J.; Li, Z.; Xu, P.; Wang, X.; Yin, W.; Wang, M.; Ge, X.; Yin, Y. Space-Confined Seeded Growth of Black Silver Nanostructures for Solar Steam Generation. *Nano Lett.* **2019**, *19*, 400–407.

(11) Shi, Y.; Li, R.; Jin, Y.; Zhuo, S.; Shi, L.; Chang, J.; Hong, S.; Ng, K. C.; Wang, P. A 3D Photothermal Structure toward Improved Energy Efficiency in Solar Steam Generation. *Joule* **2018**, *2*, 1171–1186.

(12) Liang, J.; Liu, H.; Yu, J.; Zhou, L.; Zhu, J. Plasmon–Enhanced Solar Vapor Generation. *Nanophotonics* **2019**, *8*, 771–786.

(13) Dao, V. D.; Choi, H. S. Carbon–Based Sunlight Absorbers in Solar–Driven Steam Generation Devices. *Glob. Chall.* **2018**, *2*, 1700094.

(14) Gao, M.; Zhu, L.; Peh, C. K.; Ho, G. W. Solar Absorber Material and System Designs for Photothermal Water Vaporization towards Clean Water and Energy Production. *Energy Environ. Sci.* **2019**, *12*, 841–864.

(15) Lin, X.; Chen, J.; Yuan, Z.; Yang, M.; Chen, G.; Yu, D.; Zhang, M.; Hong, W.; Chen, X. Integrative Solar Absorbers for Highly Efficient Solar Steam Generation. *J. Mater. Chem. A* **2018**, *6*, 4642–4648.

(16) Gong, F.; Li, H.; Wang, W.; Huang, J.; Xia, D.; Liao, J.; Wu, M.; Papavassiliou, D. V. Scalable, Eco–Friendly and Ultrafast Solar Steam Generators Based on One–Step Melamine–Derived Carbon Sponges toward Water Purification. *Nano Energy* **2019**, *58*, 322–330.

(17) Zhu, L.; Gao, M.; Peh, C. K. N.; Wang, X.; Ho, G. W. Self–Contained Monolithic Carbon Sponges for Solar–Driven Interfacial Water Evaporation Distillation and Electricity Generation. *Adv. Energy Mater.* **2018**, *8,* 1702149.

(18) Liu, Y.; Yu, S.; Feng, R.; Bernard, A.; Liu, Y.; Zhang, Y.; Duan, H.; Shang, W.; Tao, P.; Song, C.; Deng, T. A Bioinspired, Reusable, Paper-Based System for High–Performance Large–Scale Evaporation. *Adv. Mater.* **2015**, *27*, 2768–2774.

(19) Hogan, N. J.; Urban, A. S.; Ayala-Orozco, C.; Pimpinelli, A.; Nordlander, P.; Halas, N. J. Nanoparticles Heat through Light Localization. *Nano Lett.* **2014**, *14*, 4640–4645.

(20) Wang, X.; Liu, Q.; Wu, S.; Xu, B.; Xu, H. Multilayer Polypyrrole Nanosheets with Self-Organized Surface Structures for Flexible and Efficient Solar–Thermal Energy Conversion. *Adv. Mater.* **2019**, *31*, 1807716.

(21) Qian, X.; Zhao, Y.; Alsaid, Y.; Wang, X.; Galy, T.; Yang, Y.; Cui, J.; Liu, N.; Jiang, H.; He, X. Artificial Phototropism for Omnidirectional Tracking and Harvesting of Light. *Nat. Nanotech*. **2019**, *14*, 1048–1055.

(22) He, L,; Janner, M.; Lu, Q.; Wang, M.; Ma, H.; Yin, Y. Magnetochromatic Thin–Film Microplates. *Adv. Mater.* **2015**, *27*, 86–92.

(23) Xu, N.; Hu, X.; Xu, W.; Q. X.; Zhou, L.; Zhu, S.; Zhu, J. Mushrooms as Efficient Solar Steam Generation Devices. *Adv. Mater.* **2017**, *29*, 1606762.

(24) Li, X.; Xu, W. ; Tang, M.; Zhou, L.; Zhu, B.; Zhu, S.; Zhu, J. Graphene Oxide–Based Efficient and Scalable Solar Desalination under One Sun with A Confined 2D Water Path. *Proc. Natl. Acad. Sci. U S A* **2016**, *113*, 13953–13958.

(25) Hou, X. Smart Gating Multi-Scale Pore/Channel–Based Membranes. *Adv. Mater.* **2016**, *28*, 7049–7064.

(26) Guo, Y.; Zhao, X.; Zhao, F.; Jiao, Z.; Zhou, X.; Yu, G. Tailoring Surface Wetting States for Ultrafast Solar-Driven Water Evaporation. *Energy Environ. Sci*. **2020**. DOI: 10.1039/d0ee00399a.

(27) Zhang, L.; Tang, B.; Wu, J.; Li, R.; Wang, P. Hydrophobic Light–to–Heat Conversion Membranes with Self–Healing Ability for Interfacial Solar Heating. *Adv. Mater.* **2015**, *27*, 4889–4894.

(28) Li, X.; Ni, G.; Cooper, T.; Xu, N.; Li, J.; Zhou, L.; Hu, X.; Zhu, B.; Yao, P.; Zhu, J. Measuring Conversion Efficiency of Solar Vapor Generation. *Joule* **2019**, *3*, 1798–1803.

(29) Zhao, F.; Zhou, X.; Shi, Y.; Qian, X.; Alexander, M.; Zhao, X.; Mendez, S.; Yang, R.; Qu, L.; Yu, G. Highly Efficient Solar Vapor Generation via Hierarchically Nanostructured Gels. *Nat. Nanotech.* **2018**, *13*, 489–495.

(30) Wang, Z.; Liu, Y.; Tao, P.; Shen, Q.; Yi, N.; Zhang, F.; Liu, Q.; Song, C.; Zhang, D.; Shang, W.; Deng, T. Bio–Inspired Evaporation through Plasmonic Film of Nanoparticles at the Air-Water Interface. *Small* **2014**, *10*, 3234–3239.

(31) Zhang, P.; Liao, Q.; Yao, H.; Huang, Y.; Cheng, H.; Qu, L. Direct Solar Steam Generation System for Clean Water Production. *Energy Storage Mater.* **2019**, *18*, 429–446.

(32) Guo, Y.; Zhou, X.; Zhao, F.; Bae J.; Rosenberger B.; Yu G. Synergistic Energy Nanoconfinement and Water Activation in Hydrogels for Efficient Solar Water Desalination. *ACS Nano*. **2019**, *13*, 7913–7919.

(33) Guo, Y.; Zhao, F.; Zhou, X.; Chen, Z.; Yu, G. Tailoring Nanoscale Surface Topography of Hydrogel for Efficient Solar Vapor Generation. Nano Lett. 2019, 19, 2530–2536.

TOC Graphic:

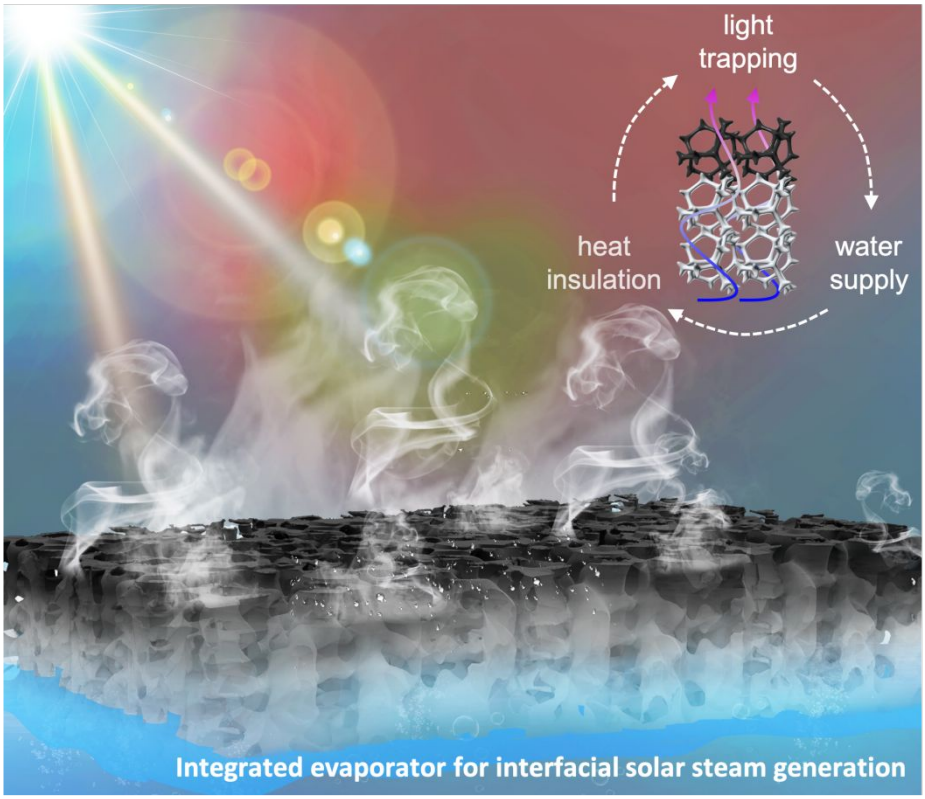
light
trapping
heat
insulation
water
supply
Integrated evaporator for interfacial solar steam generation